DRIVER-FRIENDLY EMERGENCY COLLISION AVOIDANCE SYSTEM VIA FLATNESS DIRECT YAW MOMENT CONTROL

Zejiang Wang
Walker Department of Mechanical Engineering
University of Texas at Austin
Austin, Texas 78712
wangzejiang@utexas.edu

Junmin Wang
Walker Department of Mechanical Engineering
University of Texas at Austin
Austin, Texas 78712
jwang@austin.utexas.edu

ABSTRACT

Unlike an autonomous driving system, a shared control system keeps the driver in the loop to exploit human's decision-making, path-planning, and control skills in vehicle motion control. In the meantime, a shared control system consistently provides support to the driver in hazardous situations. Typical shared control systems concentrate on altering vehicle steering actions through either active front steering or haptic steering torque. However, an active front steering system requires costly hardware and a haptic steering torque explicitly interferences with the driver hand-wheel steering. To overcome the drawbacks of the steering-based strategies, this paper introduces a driver support system based on direct yaw moment control for high-speed collision avoidance maneuvers. The new system maintains a hierarchical structure with a high-level lateral velocity planner and a low-level lateral velocity governor. In addition, the personally-preferred collision avoidance trajectories of each driver are taken into account to make the controller personalizable. Carsim-Simulink joint simulations demonstrate that this novel shared control system can successfully assist the driver in high-speed collision avoidance maneuvers. Moreover, both physical and mental loads of the driver are substantially reduced in contrast to using an active front steering system.

1   INTRODUCTION

Autonomous vehicles have the potential of revolutionizing the transportation mode in the future. However, its safety benefits will not be evident until they become commonly affordable and acceptable [1]. Besides, by isolating the human from the control loop, autonomous driving may lead to unsafe driver take-over scenarios in emergency cases. Moreover, authors in [2] indicated that autonomous driving may exacerbate passenger's fatigue instead of mitigating it. On the contrary, a shared control system keeps the driver in the loop and interacts with the driver in a cooperative manner.

Under the shared control framework, the automation system must consider the driver's intention to reduce unnecessary interferences [3] and enhance prediction accuracy of vehicle states in the near future [4]. For instance, to quantitatively analyze a driver's intent, authors in [5] demonstrated that there exists an *individually-preferred* trajectory for each specific person when he or she initiates a collision avoidance lane change. Furthermore, the *personalized* parameters of the driver steering model can be identified from historical driving data.

A high-speed lane change maneuver for collision avoidance may destabilize the vehicle and various accidents—road departure, front-end collision with another car in the target lane, side collision during lane change, etc.—may occur. To support the driver in this challenging situation, typical shared control systems focus on correcting driver's steering through either active front steering (AFS) [6] or haptic steering torque [7]. However, current commercial vehicles are in general not equipped with AFS and the haptic steering torque bluntly disturbs a driver's hand-wheel steering, which can not only deteriorate vehicle handling feeling [8] but also trigger unexpected (and probably risky) human behaviors [9].

To overcome the drawbacks of the steering-based shared control, this paper alternatively proposes a direct yaw moment control (DYC) based system for assisting the driver in high-speed collision avoidance maneuvers. This new system includes a high-level lateral velocity planner and a low-level lateral velocity controller. For the purpose of generating the desired lateral velocity, an AFS controller is designed on the basis of an extended driver-vehicle system. A linear time varying model predictive control (LTVMPC) technique is applied on the extended driver-vehicle system for determining the desired lateral velocity. Then, we take advantage of the differentially flat property of the bicycle model to determine the desired external yaw moment M_z^r, which is responsible for tracking the desired lateral velocity from the high-level planner. Actually, vehicle lateral motion control via DYC has been investigated for a very long time [10]. For example, DYC can act as a backup for steering fault-tolerate control [11]. Moreover, in contrast to AFS which needs costly hardware, DYC can be easily realized for four-wheel-drive (4WD) vehicles or vehicles equipped with in-wheel motors [12]. Furthermore, it was proved in [13] that a DYC can enhance vehicle cornering response, increase agility, and ensure stability in extreme transient operations.

The rest of the paper is organized as follows. The global control structure is depicted in Section 2. The extended driver-vehicle system modeling is illustrated and verified in Section 3. The high-level lateral velocity planner is specified in Section 4, followed by the low-level lateral velocity controller in Section 5. Simulink-Carsim joint simulations in Section 6 demonstrate the efficiency of the novel system in driver assistance. Finally, Section 7 concludes this paper.

2   CONTROL STRUCTURE

The overall architecture of the proposed shared control system for high speed collision avoidance is depicted in Fig. 1.
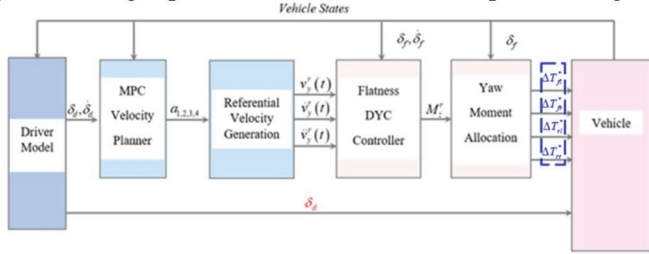

Fig. 1. Overall control scheme.

At the outset, the AFS model predictive control (MPC) lateral velocity planner utilizes vehicle states, driver hand-wheel steering angle δ_d, and hand-wheel steering rate $\dot{\delta}_d$ to decide the optimal AFS control sequence. Based upon the optimal AFS control sequence, the corresponding optimal lateral velocity series within the prediction horizon can be specified. To condense this optimal lateral velocity series, it is then converted into a third-order polynomial through a curve-fitting module. The ultimate outputs of this MPC lateral velocity planner are the coefficients a_1, a_2, a_3, a_4 of the third-order polynomial.

Subsequently, a_1, a_2, a_3, a_4 are passed through a referential velocity generation module to update not only the desired lateral velocity $v_y^r(t)$ but also its first- and second-order derivatives $\dot{v}_y^r(t), \ddot{v}_y^r(t)$ at each MPC sampling step. The referential lateral velocity signals $v_y^r(t), \dot{v}_y^r(t), \ddot{v}_y^r(t)$ are then used by the flatness DYC controller for calculating the desired external yaw moment M_z^r, which guarantees $v_y^r(t)$ tracking.

Finally, a yaw moment allocation module is designed to allocate M_z^r to four wheels' optimal extra spinning torques $\Delta T_{fl}^*, \Delta T_{fr}^*, \Delta T_{rl}^*, \Delta T_{rr}^*$. In contrast to the AFS or the haptic steering torque, the outputs of the proposed shared control system are decoupled from the driver hand-wheel steering angle δ_d to reduce the human-automation conflicts.

3   SYSTEM MODELING

When design a driver assistance system, it is beneficial to combine the vehicle dynamics with a driver behavior model. In this way, the preview accuracy of a driver's input can be improved [3], the mismatch between the predicted and actual vehicle states can be reduced [4], and the timely system intervention can be expected [7]. In this Section, we will illustrate a procedure to integrate a human steering model into a vehicle kinodynamic model, which eventually produces an extended driver-vehicle system.

3.1   COLLISION AVOIDANCE PATH

As demonstrated in [5], there exists a particularly-preferred collision avoidance trajectory for each driver in a maneuver. This trajectory can be expressed with different functions such as a polynomial [5], or a hyperbolic tangent function [14]. In this paper, the latter is chosen for its globally smooth property.

As indicated in [15], a double lane change (DLC) path can be used to describe this collision avoidance trajectory and it can be depicted as the desired lateral coordinate $Y^*(X)$ and yaw angle $\psi^*(X)$ in term of the actual longitudinal coordinate X:

$$
\begin{cases}
z_1 = st_R\left(X - X_{up}\right) - bias, \\
z_2 = st_D\left(X - X_{down}\right) - bias, \\
Y^*(X) = \dfrac{\overline{Y}\left(1+\tanh(z_1)\right) - \left(\overline{Y}-\underline{Y}\right)\left(1+\tanh(z_2)\right)}{2}, \\
\psi^*(X) = \arctan\left(dY^*(X)/dX\right).
\end{cases} \tag{1}
$$

In (1), st_R, st_D correspond to the stiffness factors, X_{up}, X_{down} indicate lane change positions, $\overline{Y}, \underline{Y}$ represent individually the upper and the lower thresholds of $Y^*(X)$, and $bias$ determines the horizontal shift of $Y^*(X), \psi^*(X)$. According to (1), the driver-preferred collision avoidance trajectory can be completely determined with seven parameters: $st_R, st_D, X_{up}, X_{down}, bias, \overline{Y}, \underline{Y}$. By using a driver simulator, the personalized results in regard to these seven parameters can be identified [14].

3.2   DRIVER STEERING MODEL

Driver steering behavior can be modeled as a feedback plus feedforward system [5], as:

$$
\begin{cases}
\delta_{dff} = K_{ff}\dot{\psi}^*\left(X_{pre}\right), \\
\delta_{dfb} + T_h\dot{\delta}_{dfb} = G_h\left(Y^*\left(X_{pre}\right) - Y_{pre}\right), \\
\delta_d = \delta_{dff} + \delta_{dfb}.
\end{cases} \tag{2}
$$

In (2), δ_{dff} and δ_{dfb} indicate separately the feedforward and the feedback parts of the driver hand-wheel steering angle. Both δ_{dff} and δ_{dfb} are defined with respect to a driver preview point $\left(X_{pre}, Y_{pre}\right)$, which can be expressed as:

$$
\begin{cases}
X_{pre} = X + v_x T_p \cos(\psi), \\
Y_{pre} = Y + v_x T_p \sin(\psi),
\end{cases} \tag{3}
$$

where (X, Y) are the actual longitudinal and lateral coordinates of the vehicle's center of gravity (CG), ψ is the actual vehicle yaw angle, v_x presents vehicle longitudinal velocity at its CG,

and T_p corresponds to the preview time. Intuitively, $v_x T_p$ is the preview distance along the vehicle heading direction.

In (2), δ_{dff} is the product of the feedforward gain K_{ff} and the desired vehicle yaw rate at the driver preview point, as:

$$\dot{\psi}^*\left(X_{pre}\right) = v_x \kappa^*\left(X_{pre}\right). \tag{4}$$

In (4), $\kappa^*\left(X_{pre}\right)$ indicates the desired road curvature on the trajectory (1) at the driver preview point (3), as:

$$\kappa^*\left(X_{pre}\right) = \frac{\partial Y^{*2}(X)}{\partial^2 X} \left/ \left(1+\left(\frac{\partial Y^*(X)}{\partial X}\right)^2\right)^{1.5}\right|_{X=X_{pre}}. \tag{5}$$

Then, δ_{dfb} in (2) can be determined according to the previewed vehicle lateral tracking error $Y^*\left(X_{pre}\right) - Y_{pre}$ at the same driver preview point (3), with:

$$Y^*\left(X_{pre}\right) = Y^*(X)\big|_{X=X_{pre}}, \tag{6}$$

being the desired lateral coordinate of the driver-preferred collision avoidance trajectory (1) when $X = X_{pre}$, and Y_{pre} being the lateral coordinate of the driver preview point, as calculated in (3). G_h, T_h in the expression of δ_{dfb} are separately the feedback gain and the first-order time constant.

Similar to the seven parameters of the driver-preferred collision avoidance trajectory in (1), K_{ff}, G_h, T_h, and T_p of a specific driver can also be identified from driving simulator experiments [5]. An exemplary driver-preferred collision avoidance trajectory, the corresponding road centerline, and the actual vehicle trajectory realized by the driver steering model (2) can be found in Fig. 2.
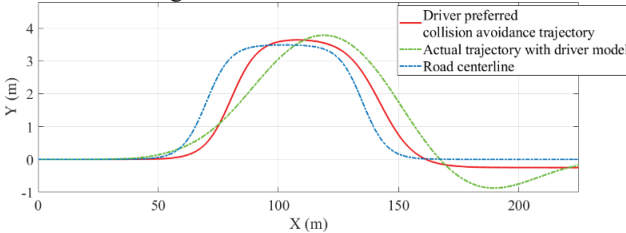

Fig. 2. Driver preferred collision avoidance trajectory.

3.3 EXTENDED DRIVER-VEHICLE SYSTEM

The vehicle longitudinal velocity is assumed constant in this paper because of two reasons: 1) The proposed DYC based shared control system has a pretty small influence on v_x. 2) Constant velocity reflects the common driver intention in highway driving scenario [16]. Therefore, a vehicle kinodynamic model can be described on the basis of the two-degree-of-freedom (2DoF) bicycle model, as:

$$\begin{cases} \dot{X} = v_x \cos(\psi) - v_y \sin(\psi), \\ \dot{Y} = v_x \sin(\psi) + v_y \cos(\psi), \\ \dot{\psi} = \gamma, \\ \dot{v}_y = F_{yf}\cos(\delta_f) + F_{yr}/m - v_x\gamma, \\ \dot{\gamma} = F_{yf}l_f\cos(\delta_f) - F_{yr}l_r/I_z. \end{cases} \tag{7}$$

In (7), X,Y are the actual longitudinal and lateral coordinates of the vehicle, ψ is vehicle yaw angle, v_x, v_y represent the longitudinal and lateral velocities at vehicle CG, γ indicates the yaw rate, l_f, l_r are separately the distance from CG to the front and the rear axle, m is the vehicle mass, and I_z is the yaw inertia. Besides, δ_f stands for the vehicle front road wheel angle and F_{yf}, F_{yr} are the lateral tire force of the front and rear axle.

If no AFS is applied and the unique steering input comes from driver hand-wheel steering angle δ_d, then we have:

$$\delta_f = \delta_d N_{ratio}, \tag{8}$$

with N_{ratio} as the steering ratio from the driver *hand-wheel* to vehicle *road* wheel.

With the nonlinear brush tire model [17], we have:

$$f_{brush\{f,r\}} = \sqrt{C_x^2\left(\frac{s_{\{f,r\}}}{s_{\{f,r\}}+1}\right)^2 + C_y^2\left(\frac{\tan\left(\alpha_{\{f,r\}}\right)}{s_{\{f,r\}}+1}\right)^2}, \tag{9}$$

$$F_{brush\{f,r\}} = \begin{cases} f_{brush\{f,r\}} - \dfrac{f_{brush\{f,r\}}^2}{3\mu F_{z\{f,r\}}} + \dfrac{f_{brush\{f,r\}}^3}{27\mu^2 F_{z\{f,r\}}^2}, f_{brush\{f,r\}} \le 3\mu F_{z\{f,r\}}, \\ \mu F_{z\{f,r\}}, f_{brush\{f,r\}} > 3\mu F_{z\{f,r\}}, \end{cases} \tag{10}$$

and

$$F_{y\{f,r\}} = -C_y \frac{\tan\left(\alpha_{\{f,r\}}\right)}{s_{\{f,r\}}+1} \frac{F_{brush\{f,r\}}}{f_{brush\{f,r\}}}, \tag{11}$$

with sideslip angle of front or rear axle as:

$$\begin{cases} \alpha_f = \arctan\left(\dfrac{v_y + l_f\gamma}{v_x}\right) - \delta_f, \\ \alpha_r = \arctan\left(\dfrac{v_y - l_r\gamma}{v_x}\right). \end{cases} \tag{12}$$

In (9) and (11), C_x, C_y represent the longitudinal and cornering stiffness of the lumped tire, $s_{\{f,r\}}$ indicate the average tire slip ratio of front and rear axle, which can be obtained through the anti-lock braking system (ABS) sensor. In (10), μ is the tire-road friction coefficient and $F_{z\{f,r\}}$ symbolizes the vertical load of the front or rear axle [17]. Although the 2DoF bicycle model with a nonlinear tire model simplifies the actual vehicle dynamics, author in [18] demonstrated that it captures the basic features of the vehicle lateral movement in emergency situations.

Finally, to integrate the driver steering model (2) with the kinodynamic vehicle model (7), the driver hand-wheel steering angle δ_d needs to be regarded as an extra system state. In other words, we have an extended state set as:

$$x = \left[X, Y, \psi, v_y, \gamma, \delta_d\right]^T, \tag{13}$$

based upon which $\dot{\delta}_d$ needs to be expressed.

By substituting (4) into (2), we have:

$$\begin{cases} \delta_{dff} = K_{ff} v_x \kappa^* \left(X_{pre} \right), \\ \delta_{dfb} + T_h \dot{\delta}_{dfb} = G_h \left(Y^* \left(X_{pre} \right) - Y_{pre} \right). \end{cases} \quad (14)$$

Hence, $\dot{\delta}_d$ can be calculated as:

$$\dot{\delta}_d = K_{ff} v_x \left. \frac{d\kappa^*(X)}{dX} \right|_{X=X_{pre}} \dot{X}_{pre} + \dot{\delta}_{dfb}. \quad (15)$$

According to (3), $\dot{X}_{pre}$ in (15) becomes:

$$\dot{X}_{pre} = \dot{X} - v_x T_p \sin(\psi)\gamma. \quad (16)$$

Also, by rearranging the second equation in (14), we have:

$$\begin{aligned} \delta_d &= \delta_{dff} + \delta_{dfb} \\ &= K_{ff} v_x \kappa^* \left(X_{pre} \right) + G_h \left(Y^* \left(X_{pre} \right) - Y_{pre} \right) - T_h \dot{\delta}_{dfb}. \end{aligned} \quad (17)$$

Finally, by multiplying both sides of (15) with T_h and then adding (15) to (17), we have:

$$\begin{aligned} \dot{\delta}_d = &-\frac{\delta_d}{T_h} + K_{ff} v_x \left. \frac{d\kappa^*(X)}{dX} \right|_{X=X_{pre}} \dot{X}_{pre} \\ &+ \frac{K_{ff} v_x \kappa^* \left(X_{pre} \right)}{T_h} + \frac{G_h \left(Y^* \left(X_{pre} \right) - Y_{pre} \right)}{T_h}. \end{aligned} \quad (18)$$

Comparison between the calculated driver handwheel steering rate (18) and the directly measured value can be found in Fig. 3, which verifies the correctness of our calculation.
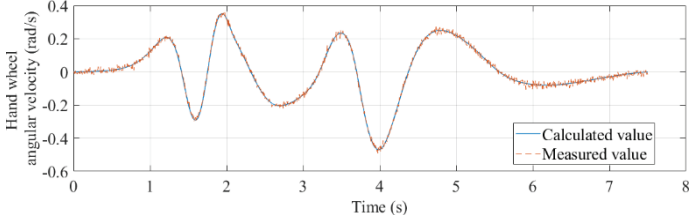

Fig. 3. Verification of calculated handwheel steering rate.

Therefore, by combining (7), (8), and (18), the extended driver-vehicle system can be compactly expressed as:

$$\dot{x} = g_{sys}(x), \quad (19)$$

with x defined in (13).

4 MPC LATERAL VELOCITY PLANNER

An AFS controller based upon the extended driver-vehicle system (19) serves as the high-level lateral velocity planner. With a unique input δ_{AFS}, the complete system of this lateral velocity planner can be expressed as:

$$\dot{x} = g_{sys}(x, u), \quad (20)$$

with $u = \delta_{AFS}$. In contrast to (8), the total vehicle front road wheel angle consequently becomes:

$$\delta_f = \delta_d N_{ratio} + u, \quad (21)$$

with N_{ratio} fixed as $1/15.176$ in this paper.

The LTVMPC technique is applied on this single-input system to determine the optimal AFS control sequence. Then, the resulting optimal lateral velocity series within the prediction horizon serves as the basis for generating the referential lateral velocity signals: $v_y^r(t), \dot{v}_y^r(t), \ddot{v}_y^r(t)$.

4.1 MPC CONSTRAINTS

The AFS controller must ensure collision avoidance, guarantee vehicle stability, consider driver comfort, and ultimately, provide referential lateral velocity signals. In accord with these requirements, the output of (20) is chosen as:

$$\eta = \begin{bmatrix} Y & \psi & \alpha_{fl} & \alpha_{fr} & \alpha_{rl} & \alpha_{rr} & v_y \end{bmatrix}^T, \quad (22)$$

with $\alpha_{i,j}, i \in \{f, r\}, j \in \{r, l\}$ as the sideslip of each tire [17].

The constraints for the AFS controller are summarized as:

$$\begin{cases} x_{k+1,t} = A_t x_{k,t} + B_t \left(u_{k-1,t} + \Delta u_{k,t} \right) + d_{k,t}, k = t \ldots t + H_p, \\ \eta_{k,t} = C_t x_{k,t} + D_t \left(u_{k-1,t} + \Delta u_{k,t} \right) + e_{k,t}, k = t \ldots t + H_p, \\ -\delta_{f\max t} \le u_{k,t} + \delta_{d_t} N_{ratio} \le \delta_{f\max t}, k = t \ldots t + H_c - 1, \\ -\Delta \delta_{f\max t} \le \Delta u_{k,t} + \Delta \delta_{d_t} N_{ratio} \le \Delta \delta_{f\max t}, k = t \ldots t + H_c - 1, \\ \alpha_{i,j\min t} - \varepsilon_{i,jt} \le \alpha_{i,jk,t} \le \alpha_{i,j\max t} + \varepsilon_{i,jt}, k = t + 1 \ldots t + H_p, \\ Y_{\min k,t} - \Upsilon_t \le Y_{k,t} \le Y_{\max k,t} + \Upsilon_t, k = t + 1 \ldots t + H_p. \end{cases} \quad (23)$$

In (23), $x_{t,t}$ represents the system's current states and $x_{k,t}, k = t + 1 \ldots t + H_p$ are the predicted states within the prediction horizon H_p. Then, $u_{k-1,t}$ indicates the applied AFS command at the last step and $\Delta u_{k,t}, k = t \ldots t + H_p$ constitute the increments of the AFS angle. We assume $\Delta u_{k,t} = 0, k = t + H_c \ldots t + H_p$, where H_c is the control horizon.

The first two equations in (23) represent individually the successively linearized system (20) as well as its output (22). A_t, B_t, C_t, D_t are the Jacobian matrices and $d_{k,t}, e_{k,t}$ indicate the linearization residues.

The third equation in (23) limits the magnitude of δ_f in (21). The magnitude of the vehicle front road-wheel angle δ_f is bounded for two purposes: 1) A large δ_f can lead to a high lateral acceleration a_y, which can affect the driver's comfort and even destabilize the vehicle. 2) A large δ_f will consume most of the available tire force, making it difficult to realize the desired external yaw moment M_z^r with a DYC [10]. By adopting the concept of safe envelop of steering wheel angle in [19], we have:

$$\delta_{f\max t} = \frac{a_{y\max}(l_f + l_r)}{v_x(t)^2} \left[1 + \frac{mv_x(t)^2(l_r - l_f)}{C_y(l_r + l_f)^2} \right], \quad (24)$$

with $a_{y\max} = \mu g$, where g is the gravity constant. C_y in (24) is still the lumped tire cornering stiffness.

Similar to the third equation, the fourth equation in (23) constrains the changing rate of δ_f to help stabilize the vehicle [18] and avoid extreme lateral jerk [20].

In the fourth equation of (23), we have:

$$\Delta u_{k,t} = u_{k,t} - u_{k-1,t}, k = t..t + H_c - 1, \quad (25)$$

as the increments of the AFS in the control horizon. What's more,

$$\Delta \delta_{d_t} = \dot{\delta}_d T_s, \quad (26)$$

implies the increment of driver hand-wheel steering angle at the current step, with T_s being the sampling period of the LTVMPC and $\dot{\delta}_d$ as the driver hand-wheel steering rate from (18).

Like (24), $\Delta \delta_{f \max t}$ can be calculated as:

$$\Delta \delta_{f \max t} = \frac{\dot{a}_{y \max} \left(l_f + l_r \right)}{v_x \left(t \right)^2} \left[1 + \frac{m v_x \left(t \right)^2 \left(l_r - l_f \right)}{2 C_y \left(l_r + l_f \right)^2} \right] T_s, \quad (27)$$

where $\dot{a}_{y \max} = 30 m/s^3$ for a sharp lane change [21].

The fifth equation in (23) restrains the four tires' sideslip angles to ensure the stability of the vehicle. The upper and lower bounds $\alpha_{i,j \max t}, \alpha_{i,j \min t}$ are chosen according to the adaptive threshold on the tire sideslip in [17].

Finally, the last equation in (23) limits the vehicle lateral coordinate within the prediction horizon. As illustrated in [22], either static or moving obstacles give us a drivable tubes. By enforcing the predicted vehicle trajectory to always lay within one of the drivable tubes, a collision-free trajectory can be found in real-time. The idea is illustrated in Fig. 4.
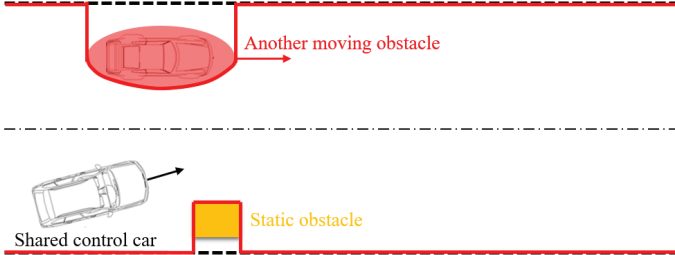

Fig. 4. A drivable tube.

In Fig. 4, the ego-car initiates a DLC for avoiding a static obstacle in front. In the meantime, there exists a moving obstacle in the adjacent lane. The bold red lines depict the bounds of a drivable tube. We assume that the CG of the moving obstacle can be measured. Also, to account for sensor errors, an error ellipse [23] is used to expand the size of the moving obstacle. For the sake of simplicity, we assume the physical size of the moving obstacle is akin to the size of the shared control car. Thus, the mathematical expression of the error ellipse $\left(X_e, Y_e \right)$ around the moving obstacle can be fixed as:

$$\frac{\left(X_e - X_{obs} \left(t \right) \right)^2}{\left(l_f + l_r \right)^2} + \frac{\left(Y_e - Y_{obs} \left(t \right) \right)^2}{\left(1.5 l_d \right)^2} = 1, \quad (28)$$

where $\left(X_{obs} \left(t \right), Y_{obs} \left(t \right) \right)$ represent the measured longitudinal and lateral coordinates of the obstacle, l_d shows the ego-car's half-track, and $l_f + l_r$ equals the wheelbase of the ego-car.

At each MPC update step, the shared control car predicts its longitudinal coordinate $X_{k,t}$. Then, it determines the bound of its predicted lateral coordinate at each step within the prediction horizon as follows.

If $X_{obs} \left(t \right) - l_f - l_r \leq X_{k,t} \leq X_{obs} \left(t \right) + l_f + l_r$, then $Y_{\max k,t}$ is constrained by the lower boundary of the error ellipse. Else, $Y_{\max k,t}$ must be restricted by the upper road boundary. As for $Y_{\min k,t}$, it is simplified as the lower road boundary because the static obstacle can always be dodged by the driver steering model (2) even without the AFS intervention.

To ensure feasibility of the MPC, the last two constraints in (23) are set soft with slackness variables $\varepsilon_{i,jt}$ and Υ_t.

4.2   MPC COST FUNCTION

The cost function of the LTVMPC is formulated as:

$$\min_{\Delta U, \varepsilon_{i,jt}, \Upsilon_t} J \left(x_{t,t}, \Delta U, \varepsilon_{i,jt}, \Upsilon_t \right), \quad (29)$$

with $\Delta U = \Delta u_{k,t}, k = t..t + H_c - 1$, and the expression of J is:

$$J \left(x_{t,t}, \Delta U, \varepsilon_{i,jt}, \Upsilon_t \right) = \sum_{j=1}^{H_p} \left\| \psi_{t+j,t} - \psi_{t+j,t}^* \right\|_{Q_\psi}^2 +$$

$$\sum_{j=1}^{H_p} \left\| Y_{t+j,t} - Y_{t+j,t}^* \right\|_{Q_Y}^2 + \sum_{i=0}^{H_c - 1} \left\| u_{t+i,t} \right\|_S^2 + \sum_{i=0}^{H_c - 1} \left\| \Delta u_{t+i,t} \right\|_R^2 \quad (30)$$

$$+ \sum_{i=right}^{left} \sum_{j=front}^{rear} \left\| \varepsilon_{i,jt} \right\|_{\rho_{i,j}}^2 + \left\| \Upsilon_t \right\|_G^2$$

In (30), the first and the second terms penalize the yaw angle and the lateral coordinate tracking errors in regard to the driver-preferred collision avoidance trajectory (1). The third term limits the magnitude of the intrusive AFS while the fourth term constraints the increment of the AFS. And the last two terms correspond to the soft constraints' violation penalties.

To decide the weighting matrices $Q_\psi, Q_Y, S, R, \rho_{i,j}, G$ in (30), the range-based MPC tuning rule in [24] is adopted.

Specifically speaking, Q_ψ, Q_Y are respectively the range of the yaw angle and the lateral coordinate of the driver-preferred collision avoidance trajectory, as:

$$\begin{cases} Q_\psi = \max \left(\psi^* \left(X \right) \right) - \min \left(\psi^* \left(X \right) \right), \\ Q_Y = \max \left(Y^* \left(X \right) \right) - \min \left(Y^* \left(X \right) \right), \end{cases} \quad (31)$$

where $Y^* \left(X \right), \psi^* \left(X \right)$ are described in (1).

Then, according to the third equation in (23), we have:

$$-\delta_{f \max t} - \delta_{d_t} N_{ratio} \leq u_{k,t} \leq \delta_{f \max t} - \delta_{d_t} N_{ratio}, \quad (32)$$

with $\delta_{f \max t}$ being defined in (24). Consequently, a penalty matrix S can be naturally determined as:

$$S = 2 \delta_{f \max}. \quad (33)$$

In a similar manner, we have:

$$R = 2 \Delta \delta_{f \max t}, \quad (34)$$

with $\Delta \delta_{f \max t}$ defined in (27).

Afterward, the weight coefficient $\rho_{i,j}$ in regard to violation of the soft constraint on tire sideslip angle is designed as:

$$\rho_{i,j} = \tan\left(\frac{\pi}{2}\left(1 - \frac{\partial F_{brushi,j}}{\partial f_{brushi,j}}\right)\right), \qquad (35)$$

where $F_{brushi,j}$ and $f_{brushi,j}$ come from the identical brush model (9)-(11), but applied on each single tire. Details on $F_{brushi,j}$ and $f_{brushi,j}$ can be found in [17]. The relationship between the weight coefficient $\rho_{i,j}$ and the tire force usage $f_{brushi,j}$ is depicted in Fig. 5.
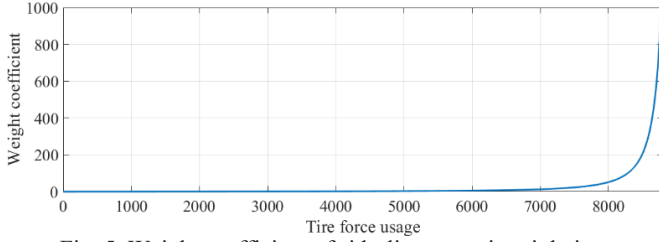
Fig. 5. Weight coefficient of sideslip constraint violation.

As demonstrated in Fig. 5, when the tire force usage $f_{brushi,j}$ approaches to the saturation limit $3\mu F_{zi,j}$, the corresponding $\rho_{i,j}$ drastically increases. This intense enhancement of $\rho_{i,j}$ can restrain the tire sideslip angle $\alpha_{i,j}$ from entering into the saturated region and preserve the stability of the vehicle.

Finally, G—the weight coefficient with regard to the violation of the soft constraint on vehicle lateral coordinate—is simply fixed as an extremely large constant, because collision avoidance must have the highest priority among all the control objectives in (30).

4.3 LATERAL VELOCITY GENERATION

After solving the optimization problem (29) under multiple constraints (23), the optimal AFS control increment sequence: $\Delta u_{k,t}^*, k = t...t + H_c - 1$ can be obtained. For a special vehicle equipped with an AFS, it can be directly used for shared control. However, as we emphasized in Section 1, AFS is in general not available for most passenger cars.

Instead, $\Delta u_{k,t}^*$ is then substituted back into the first equation of (23) to decide the optimal predicted state series: $x_{k,t}^*, k = t+1...t + H_p$. As indicated in (13), we can then isolate $v_{yk,t}^*, k = t+1...t + H_p$ from other states.

To condense the useful information within $v_{yk,t}^*, k = t+1...t + H_p$, a third-order polynomial curve fitting is applied to fit $v_{yk,t}^*$ with respect to the corresponding time stamp sequence: $\tau + T_s...\tau + H_p T_s$, with τ as the current time stamp.

The fitted result is the desired lateral velocity, as:

$$v_y^r(t) = a_1 t^3 + a_2 t^2 + a_3 t + a_4, t \in [\tau, \tau + H_p T_s]. \qquad (36)$$

From (36), the first-order and second-order derivatives of $v_y^r(t)$ can be determined, as:

$$\begin{cases} \dot{v}_y^r(t) = 3a_1 t^2 + 2a_2 t + a_3, t \in [\tau, \tau + H_p T_s], \\ \ddot{v}_y^r(t) = 6a_1 t + 2a_2, t \in [\tau, \tau + H_p T_s]. \end{cases} \qquad (37)$$

The coefficients a_1, a_2, a_3, a_4 in (36) are updated at each MPC sampling step. Between two consecutive sampling steps, they are regarded as constant.

5 FLATNESS DYC CONTROLLER

The objective of the low-level DYC controller is to generate the desired external yaw moment M_z^r for tracking the desired lateral velocity $v_y^r(t)$. The differentially flat property of the 2DoF bicycle model is exploited to facilitate controller design.

5.1 DIFFERENTIAL FLATNESS SYSTEM

A dynamic system $\dot{x} = f(x,u)$ with $x \in \mathbb{R}^n$ and $u \in \mathbb{R}^m$ is differentially flat [25] if there exists a set of variables, $y = h(x,u,\dot{u},...,u^{(r)}), y \in \mathbb{R}^m, r \in \mathbb{N}$, called a flat output, such that $x = \Lambda(y,\dot{y},...,y^{(v_x)}), u = \Theta(y,\dot{y},...,y^{(v_u)})$, with Λ and Θ being either linear or nonlinear functions, which satisfy:
$d\Lambda(y,\dot{y},...,y^{(q+1)})/dt = f(\Lambda(y,\dot{y},...,y^{(q)}), \Theta(y,\dot{y},...,y^{(q+1)}))$, with $q \in \mathbb{N}$.

If a nonlinear system is differentially flat, then it can be exactly linearized with respect to the flat output.

5.2 FLATNESS CONTROLLER DESIGN

As proved in [26], by treating the vehicle front road wheel angle δ_f as a measurable parameter and the desired external yaw moment M_z^r as the *unique* system input, then the 2DoF bicycle model:

$$\begin{cases} \dot{v}_y = \dfrac{F_{yf}\cos(\delta_f) + F_{yr}}{m} - v_x\gamma, \\ \dot{\gamma} = \dfrac{F_{yf}l_f\cos(\delta_f) - F_{yr}l_r + M_z^r}{I_z}, \end{cases} \qquad (38)$$

is a differentially flat system with the flat output as v_y.

Based on the brush tire model (9)-(11), the lateral tire forces of front and rear axle can be compactly expressed as:

$$F_{y\{f,r\}} = g_1\left(\mu, F_{z\{f,r\}}, \alpha_{\{f,r\}}, s_{\{f,r\}}\right). \qquad (39)$$

In (39), μ is supposed to be constant. Also, $F_{z\{f,r\}}$ remains almost unchanged owing to a negligible load transfer from the constant v_x. Finally, we ignore the derivatives of tire slip ratios $s_{\{f,r\}}$ due to the relatively fast wheel dynamics.

With the above three simplifications, we can follow the method in [26] to find the linear affine relationship between the

second order derivative of the flat output v_y and the unique system input M_z^r, as:

$$\ddot{v}_y = A_{flat} + B_{flat} M_z^r, \qquad (40)$$

with

$$
\begin{aligned}
&A_{flat}\\
&= \frac{\dfrac{1}{m}\dfrac{\partial F_{yf}}{\partial \alpha_f}\cos(\delta_f)\left[-v_x^2\gamma + v_x\left(\dfrac{\cos(\delta_f)}{m} + \dfrac{l_f^2\cos(\delta_f)}{I_z}\right)F_{yf}\right]}{v_x^2 + (v_y + l_f\gamma)^2}\\[6pt]
&\quad -\frac{1}{m}\frac{\partial F_{yf}}{\partial \alpha_f}\cos(\delta_f)\dot{\delta}_f + \frac{\dfrac{v_x}{m}\dfrac{\partial F_{yf}}{\partial \alpha_f}\cos(\delta_f)\left(\dfrac{1}{m} - \dfrac{l_f l_r}{I_z}\right)F_{yr}}{v_x^2 + (v_y + l_f\gamma)^2}\\[6pt]
&\quad + \frac{\dfrac{1}{m}\dfrac{\partial F_{yr}}{\partial \alpha_r}\left[-v_x^2\gamma + v_x\left(\dfrac{\cos(\delta_f)}{m} - \dfrac{l_f l_r\cos(\delta_f)}{I_z}\right)F_{yf}\right]}{v_x^2 + (v_y - l_r\gamma)^2}\\[6pt]
&\quad + \frac{\dfrac{\partial F_{yr}}{\partial \alpha_r}v_x\left(\dfrac{1}{m} + \dfrac{l_r^2}{I_z}\right)F_{yr}}{m\left(v_x^2 + (v_y - l_r\gamma)^2\right)} - \frac{v_x F_{yf}\cos(\delta_f)l_f}{I_z}\\[6pt]
&\quad + \frac{v_x F_{yr}l_r}{I_z} - \frac{F_{yf}}{m}\sin(\delta_f)\dot{\delta}_f, \qquad (41)
\end{aligned}
$$

and

$$B_{flat} = \frac{\dfrac{\partial F_{yf}}{\partial \alpha_f}\cos(\delta_f)v_x l_f}{mI_z\left(v_x^2 + (v_y + l_f\gamma)^2\right)} - \frac{\dfrac{\partial F_{yr}}{\partial \alpha_r}v_x l_r}{mI_z\left(v_x^2 + (v_y - l_r\gamma)^2\right)} - \frac{v_x}{I_z}. \qquad (42)$$

In (41) and (42), the vehicle front road wheel angle δ_f can be directly measured according to (8) and its derivative is $\dot{\delta}_f = \dot{\delta}_d N_{ratio}$, where $\dot{\delta}_d$ comes from (18).

According to the linear affine relationship in (40), it becomes straightforward to design the desired external yaw moment M_z^r as:

$$M_z^r = \frac{\ddot{v}_{yr} + K_1\left(\dot{v}_y - \dot{v}_{yr}\right) + K_0\left(v_y - v_{yr}\right) - A_{flat}}{B_{flat}}. \qquad (43)$$

In (43), $v_{yr}, \dot{v}_{yr}, \ddot{v}_{yr}$ are the referential lateral velocity signals from (36) and (37). Time index (t) is omitted for brevity.

By substituting (43) back into (40) and assigning $e_{v_y} = v_y - v_{yr}$, we have:

$$\ddot{e}_{v_y} = K_1 \dot{e}_{v_y} + K_0 e_{v_y}. \qquad (44)$$

Or equivalently,

$$\begin{bmatrix} \dot{e}_{v_y} \\ \ddot{e}_{v_y} \end{bmatrix} = \begin{bmatrix} 0 & 1 \\ K_0 & K_1 \end{bmatrix}\begin{bmatrix} e_{v_y} \\ \dot{e}_{v_y} \end{bmatrix}. \qquad (45)$$

The eigenvalues of the system matrix in (45) can be expressed as:

$$\lambda_1 = \frac{K_1 + \sqrt{K_1^2 + 4K_0}}{2}, \quad \lambda_2 = \frac{K_1 - \sqrt{K_1^2 + 4K_0}}{2}. \qquad (46)$$

By making the real parts of λ_1, λ_2 strictly negative, we have $\lim\limits_{t\to\infty} v_y(t) \to v_{yr}(t)$. To treat the system uncertainty, it is preferable to make the real parts of λ_1, λ_2 far less than zero. However, in this way, the generated M_z^r may be too large to be tracked.

5.3 EXTERNAL YAW MOMENT ALLOCATION

The desired external yaw moment from (43) needs to be allocated to the four wheels' optimal extra spinning torques. Typical approaches of yaw moment allocation include pseudo-inverse [27], [28] and numerical optimization [29]. In this paper, the pseudo-inverse method is preferred for its slight computational burden.

To begin with, we can establish the relationship between any given external yaw moment M_z and the added four wheels' longitudinal tire forces: $\Delta F_X = \begin{bmatrix} \Delta F_{xfl}, \Delta F_{xfr}, \Delta F_{xrl}, \Delta F_{xrr} \end{bmatrix}^T$ as:

$$M_z = G\Delta F_X, \qquad (47)$$

where

$$G = \begin{bmatrix} -\cos(\delta_f)l_d + \sin(\delta_f)l_f, \cos(\delta_f)l_d + \sin(\delta_f)l_f, -l_d, l_d \end{bmatrix}. \qquad (48)$$

Thereafter, we can design a cost function for allocating M_z^r in (43) into ΔF_X, as:

$$J_{M_z^r} = \Delta F_X^T W \Delta F_X + \left(G\Delta F_X - M_z^r\right)^T H \left(G\Delta F_X - M_z^r\right). \qquad (49)$$

In (49), the first term aims at constraining excessive ΔF_X and the second term is responsible for restricting the allocation error. W in (49) is chosen as a 4*4 diagonal matrix with the diagonal elements as:

$$
\begin{aligned}
w_{11} &= \frac{\max\left(F_{xfl}^{\max}, F_{xfr}^{\max}, F_{xrl}^{\max}, F_{xrr}^{\max}\right)}{F_{xfl}^{\max}}, \quad
w_{22} = \frac{\max\left(F_{xfl}^{\max}, F_{xfr}^{\max}, F_{xrl}^{\max}, F_{xrr}^{\max}\right)}{F_{xfr}^{\max}},\\[6pt]
w_{33} &= \frac{\max\left(F_{xfl}^{\max}, F_{xfr}^{\max}, F_{xrl}^{\max}, F_{xrr}^{\max}\right)}{F_{xrl}^{\max}}, \quad
w_{44} = \frac{\max\left(F_{xfl}^{\max}, F_{xfr}^{\max}, F_{xrl}^{\max}, F_{xrr}^{\max}\right)}{F_{xrr}^{\max}}.
\end{aligned} \qquad (50)
$$

In (50), $F_{xij}^{\max}$ is the maximum available longitudinal tire force of each wheel, as:

$$F_{xij}^{\max} = \sqrt{\left(\mu F_{zij}\right)^2 - F_{yij}^2}, \qquad (51)$$

where F_{yij}, F_{zij} represent individually the lateral and vertical tire force of each wheel [17].

Then, H in (49) is designed as:

$$H = \phi \max\left(w_{11}, w_{22}, w_{33}, w_{44}\right), \phi \in \mathbb{R}, \phi \gg 1, \qquad (52)$$

to guarantee a small allocation error.

As a canonical quadratic programming problem, (49) can be analytically solved. The optimally added four wheels' longitudinal tire forces become:

$$\Delta F_X^* = \left(W + G^T H G\right)^{-1} G^T H M_z^r. \qquad (53)$$

Finally, by omitting wheel dynamics, four wheels' optimal extra spinning torques can be calculated as:

$$\Delta T_{add}^{*} = \Delta F_{X}^{*} R_{ew}, \qquad (54)$$

where R_{ew} stands for effective wheel radius. ΔT_{add}^{*} in (54) is a 4*1 column, and its first, second, third, and last element correspond individually to $\Delta T_{fl}^{*}, \Delta T_{fr}^{*}, \Delta T_{rl}^{*}, \Delta T_{rr}^{*}$ in Fig. 1.

6 SIMULATION RESULTS

A collision-avoidance scenario with a moving obstacle is created to verify the effectiveness of the novel DYC based shared control system. As depicted in Fig. 4, the shared control car initiates a DLC maneuver for avoiding the static obstacle ahead. However, there exists another moving vehicle in the adjacent lane. Hence, the shared-control vehicle must also avoid a side collision during lane change.

Vehicle parameters were set as: $C_x = 66900N$, $C_y = 62700N/rad$, $l_f = 1.232m$, $l_r = 1.468m$, $m = 1723kg$, $l_d = 0.77m$, $I_z = 1960kg \cdot m^2$, $R_{ew} = 0.31m$. The high-level MPC controller was tuned with $T_s = 0.05s$, $N_p = 30$, $N_c = 2$. The gains in (44) were chosen as: $K_1 = -24$, $K_0 = -144$, and ϕ in (52) was set as 10. To realize a shared control structure, driver's hand-wheel steering angle δ_d was generated according to the driver steering model (2) with parameters set as: $K_{ff} = 0.15$, $G_h = 0.15$, $T_h = 0.3$, $T_p = 1.0$. Besides, tire road friction coefficient was set as $\mu = 0.75$. Finally, vehicle longitudinal velocity was chosen as $v_x = 70mph$.

6.1 HIGH LEVEL AFS VERIFICATION

Firstly, we verify that the LTVMPC lateral velocity planner in Section 4 works properly. By solving the optimization problem (29) under the constraints (23), we can obtain the optimal AFS control sequence. At each MPC sampling step, the first element in this sequence was virtually applied on the shared control vehicle. The optimal AFS angle as well as its increment is drawn in Fig. 6.
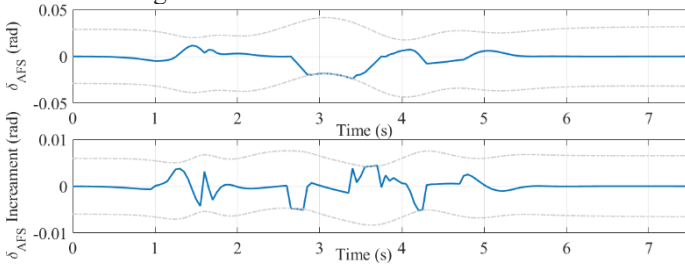

Fig. 6. AFS magnitude and increment constraints.

As indicated in Fig. 6, both the AFS angle and its increment observed the third and the fourth constraints in (23).

Then, the sideslip angle of each wheel is exhibited in Fig. 7. The red dashed lines correspond to the adaptive sideslip thresholds, as indicated in [17]. Therefore, all four tires' sideslip angles respected the fifth constraint in (23).
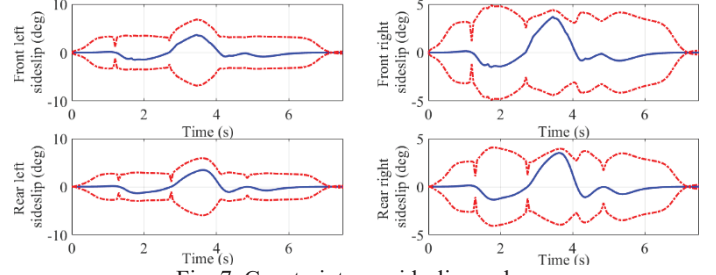

Fig. 7. Constraints on sideslip angles.

6.2 HIERARCHICAL STRUCTURE VERIFICATION

In this Section, the complete shared-control structure in Fig. 1 is verified.

Firstly, the referential lateral velocity signals $v_y^r(t), \dot{v}_y^r(t), \ddot{v}_y^r(t)$ from (36) and (37) are depicted in Fig. 8.
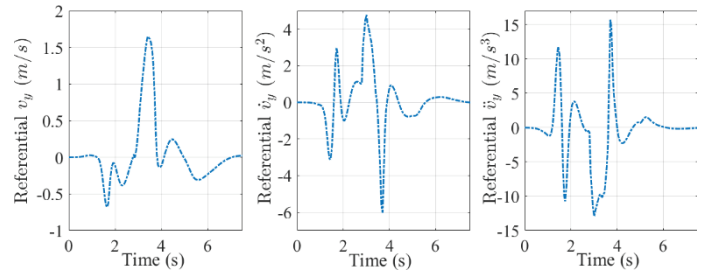

Fig. 8. Referential velocities generation.

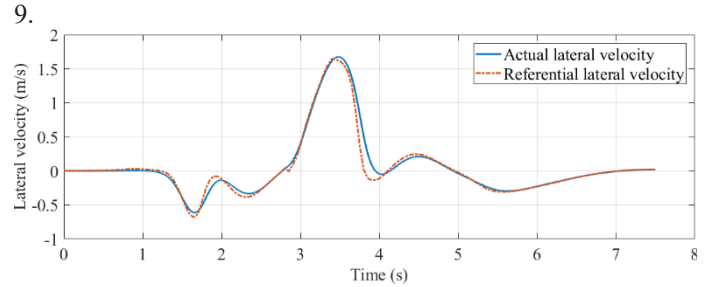Then, the lateral velocity tracking result is depicted in Fig. 9.

Fig. 9. Lateral velocity tracking with flatness DYC.

As shown in Fig. 9, the actual lateral velocity closely followed the desired lateral velocity. The tracking error did exist, principally due to the modelling errors.

Subsequently, the four wheels' optimal extra spinning torques in (54) are shown in Fig. 10. For a four-wheel independent actuated (4WIA) vehicle [28], the extra spinning torque of each wheel can be implemented by individually control the respective in-wheel motor.
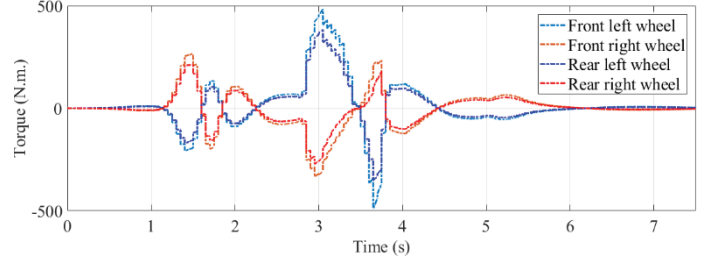

Fig. 10. Allocated four wheels' torques.

As stated in Fig. 10, extra wheel spinning torques produced by DYC had approximately the same magnitude but opposite sign on the right and left sides of the vehicle, which justified the assumption that the longitudinal velocity v_x can be roughly regarded as constant.

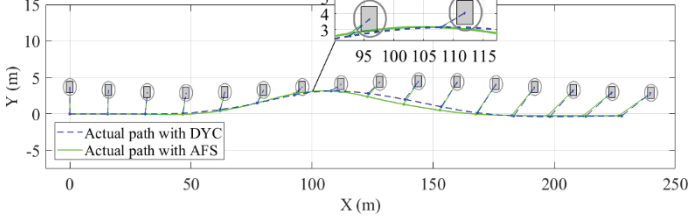Finally, the collision avoidance trajectories by AFS and DYC intervention are compared in Fig. 11.

Fig. 11. Collision avoidance trajectory comparison.

In Fig. 11, the green solid line corresponds to the trajectory when AFS command was directly applied on the shared-control vehicle. The blue dashed line represents the resulting trajectory with DYC allocation. The gray rectangle with a surrounding ellipse represented the moving obstacle. For demonstration purpose, the CGs of the obstacle and the shared-control vehicle were connected together via a straight line. Clearly, both AFS and DYC can help the shared-control car avoid the side collision. Although the AFS controller gave us a more damped trajectory, AFS, as we emphasized in Section 1, is not a standard actuator for current commercial vehicles.

6.3 DRIVER WORKLOAD COMPARISON

The driver hand-wheel steering angle δ_d and steering rate $\dot{\delta}_d$ with either AFS or DYC intervention are compared in Fig. 12.
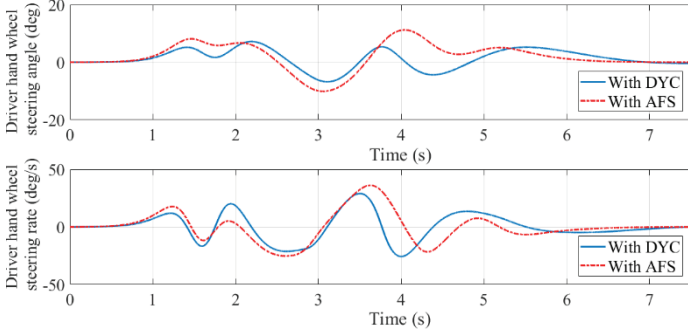

Fig. 12. Driver input with either AFS or DYC intervention.

As described in Fig. 12, both δ_d and $\dot{\delta}_d$ became smoother by the use of DYC. Furthermore, as explained in [30], the driver's physical load and mental load within a time period $[0, T]$ can be quantified as:

$$\begin{cases} L_{physical} = \int_0^T \delta_d(t)^2 \, dt \Big/ T, \\ L_{mental} = \int_0^T \dot{\delta}_d(t)^2 \, dt \Big/ T. \end{cases} \quad (55)$$

The driver physical and mental loads with either AFS or DYC intervention are summarized in Table. 1.

Table 1 Driver workloads

	$L_{mental} \left(\deg / s \right)^2$	$L_{physical} \left(\deg \right)^2$
DYC	136.1	12.1
AFS	164.0	25.0

According to Table 1, the DYC can effectively lessen the driver's physical and mental loads. The mental load was reduced more than 17% and the physical load was even reduced more than 51% with respect to AFS. This is because that the DYC eliminates the explicit human-machine conflict by decoupling the system intervention from driver hand-wheel steering.

7 CONCLUSIONS

This paper proposes a novel shared control system for assisting driver in high speed collision-avoidance maneuvers. The new system maintains a hierarchical structure with a high-level MPC based lateral velocity planner and a low-level flatness DYC lateral velocity controller. Simulation results demonstrate the efficiency of this new system. Compared with an prohibitively expensive AFS controller, the proposed system can substantially reduce the driver workloads. Furthermore, this novel shared control system uses driver-preferred collision avoidance trajectory and extended driver-vehicle system to account for driver's intention, which makes it personalizable.

Future work will concentrate on driver adaption issue, system robustness, and actuator constraints.

REFERENCES
[1] Litman, T. "Autonomous Vehicle Implementation Predictions Implications for Transport Planning." Victoria Transp. Policy Inst., Victoria, BC, Canada, 2014.
[2] Merat, N. and Lee, J.D. "Preface to The Special Section on Human Factors and Automation in Vehicles: Designing Highly Automated Vehicles with the Driver in Mind." *Human Factors*, Vol. 54 No.5 (2012): pp. 681-686.
[3] Saleh, L., Chevrel, P., Claveau, F., Lafay, J.F. and Mars, F. "Shared Steering Control Between a Driver and an Automation: Stability in the Presence of Driver Behavior Uncertainty." *IEEE Transactions on Intelligent Transportation Systems*, Vol. 14 No.2 (2013): pp. 974-983.
[4] Vasudevan, R., Shia, V., Gao, Y., Cervera-Navarro, R., Bajcsy, R. and Borrelli, F. "Safe semi-autonomous control with enhanced driver modeling." *American Control Conference (ACC)*. pp. 2896-2903. Fairmont Queen Elizabeth, Montréal, Canada, June 27-29, 2012.
[5] Schnelle, S., Wang, J., Su, H.J and Jagacinski, R. "A Personalizable Driver Steering Model Capable of Predicting Driver Behaviors in Vehicle Collision Avoidance Maneuvers." *IEEE Transactions on Human-Machine Systems*, Vol. 47 No.5 (2017): pp. 625-635.
[6] Ji, J., Khajepour, A., Melek, W.W. and Huang, Y. "Path Planning and Tracking for Vehicle Collision Avoidance

Based on Model Predictive Control with Multiconstraints." *IEEE Transactions on Vehicular Technology*, Vol. 66 No.2 (2017): pp. 952-964.

[7] Ercan, Z., Carvalho, A., Tseng, H.E., Gökaşan, M. and Borrelli, F. "A Predictive Control Framework for Torque-Based Steering Assistance to Improve Safety in Highway Driving." *Vehicle System Dynamics*, Vol. 56 No.5 (2018): pp.810-831.

[8] Zafeiropoulos, S. and Di Cairano, S. "Vehicle Yaw Dynamics Control by Torque-Based Assist Systems Enforcing Driver's Steering Feel Constraints." *American Control Conference (ACC).* pp. 6746-6751. Washington, DC, USA, June 17-19, 2013.

[9] Iwano, K., Raksincharoensak, P. and Nagai, M. "A Study on Shared Control between the Driver and an Active Steering Control System in Emergency Obstacle Avoidance Situations." *Proc. 19th World Congr. Int. Fed. Autom. Control.* pp. 6338-6343. Cape Town, South Africa. August 24-29, 2014.

[10] Pilutti, T., Ulsoy, G. and Hrovat, D. "Vehicle Steering Intervention Through Differential Braking." *Journal of Dynamic Systems, Measurement, and Control*, Vol. 120 No. 2 (1998): pp.314-321.

[11] Wang, R., Jing, H., Hu, C., Chadli, M. and Yan, F. "Robust H∞ Output-Feedback Yaw Control for In-Wheel Motor Driven Electric Vehicles with Differential Steering." *Neurocomputing*, Vol. 173 (2016): 676-684.

[12] Kirli, A., Okwudire, C.E. and Ulsoy, A.G. "Limitations of Torque Vectoring as a Backup Safety Strategy for Steer-by-Wire Vehicles due to Vehicle Stability Control." *Proceedings of the ASME 2017 Dynamic Systems and Control Conference (DSCC).* DSCC2017-5190: pp. V001T45A008-V001T45A008. Tysons, Virginia, USA, Oct. 11-13, 2017.

[13] Chatzikomis, C., Sorniotti, A., Gruber, P., Zanchetta, M., Willans, D. and Balcombe, B. "Comparison of Path Tracking and Torque-Vectoring Controllers for Autonomous Electric Vehicles." *IEEE Transactions on Intelligent Vehicles*, Vol. 3 No.4 (2018): pp.559-570.

[14] Schnelle, S., Wang, J., Su, H., and Jagacinski, R. "A Driver Steering Model with Personalized Desired Path Generation." *IEEE Transactions on Systems, Man, and Cybernetics: Systems*, Vol. 47 No.1 (2017): pp.111-120.

[15] Falcone, P., Borrelli, F., Asgari, J., Tseng, H.E. and Hrovat, D. "Predictive Active Steering Control for Autonomous Vehicle Systems." *IEEE Transactions on Control Systems Technology*, Vol. 15 No.3 (2007): pp.566-580.

[16] Anderson, S., Peters, S., Iagnemma, K., and Overholt, J. "Semi-Autonomous Stability Control and Hazard Avoidance for Manned and Unmanned Ground Vehicles." *27th Army Science Conference*. pp. 1-8. Orlando, FL, USA. Nov 29-Dec 02, 2010.

[17] Wang, Z., Bai, Y., Wang, J., and Wang, X. "Vehicle Path Tracking LTV-MPC Controller Parameter Selection Considering CPU Computational Load," *Journal of Dynamic Systems, Measurement, and Control*, Vol. 141 (2019): pp. 051004-1-12.

[18] Funke, J. "Collision Avoidance Up to the Handling Limits for Autonomous Vehicles." PhD Thesis. Stanford University, Standford, CA. 2015

[19] Tan, D., Chen, W., Wang, H. and Gao, Z. "Shared Control for Lane Departure Prevention Based on The Safe Envelope of Steering Wheel Angle." *Control Engineering Practice*, Vol. 64 (2017): pp.15-26.

[20] Hatipoglu, C., Ozguner, U. and Redmill, K.A. "Automated Lane Change Controller Design." *IEEE Transactions on Intelligent Transportation Systems*, Vol. 4 No. 1 (2003): pp.13-22.

[21] Isermann, R., Stählin, U. and Schorn, M. "Collision Avoidance System Proreta-Strategies Trajectory Control and Test Drives." *5th International Conference on Informatics in Control, Automation and Robotics (ICINCO-ICSO)*: pp. 35-42. Funchal, Madeira, Portugal.

[22] Erlien, S.M., Fujita, S. and Gerdes, J.C. "Shared Steering Control Using Safe Envelopes for Obstacle Avoidance and Vehicle Stability." *IEEE Transactions on Intelligent Transportation Systems*, Vol. 17 No.2 (2016): pp.441-451.

[23] Mousavi, M.A., Heshmati, Z. and Moshiri, B. "LTV-MPC Based Path Planning of an Autonomous Vehicle via Convex Optimization." *21st Iranian Conference on Electrical Engineering (ICEE)*: pp. 1-7. Mashhad, Iran, May 14-16, 2013.

[24] Garriga, J.L. and Soroush, M. "Model Predictive Control Tuning Methods: A Review." *Industrial and Engineering Chemistry Research*, Vol. 49 No.8 (2010): pp. 3505-3515.

[25] Fliess, M., Lévine, J., Martin, P. and Rouchon, P. "Flatness and Defect of Non-Linear Systems: Introductory Theory and Examples." *International Journal of Control*, Vol. 61 No. 6 (1995): pp.1327-1361

[26] Antonov, S., Fehn, A. and Kugi, A. "A New Flatness-Based Control of Lateral Vehicle Dynamics." *Vehicle System Dynamics*, Vol. 46 No.9 (2008): pp.789-801.

[27] Wang, J. and Longoria, R.G. "Coordinated Vehicle Dynamics Control with Control Distribution." *American Control Conference (ACC).* pp. 5348-5353. Minneapolis, MN, USA, June 14-16, 2006.

[28] Wang, R., Hu, C., Wang, Z., Yan, F. and Chen, N. "Integrated Optimal Dynamics Control of 4WD4WS Electric Ground Vehicle with Tire-Road Frictional Coefficient Estimation." *Mechanical Systems and Signal Processing*, Vol. 60 (2015): pp.727-741.

[29] Wang, J. and Longoria, R.G. "Coordinated and Reconfigurable Vehicle Dynamics Control." *IEEE Transactions on Control Systems Technology*, Vol.17 No.3 (2009): pp.723-732.

[30] Wang, W., Xi, J. and Wang, J. "Human-centered feed-forward control of a vehicle steering system based on a driver's steering model." *American Control Conference (ACC).* pp. 3361-3366. Chicago, IL, USA, July 1-3, 2015.